

1      **High-level cognition during story listening is reflected in  
2      high-order dynamic correlations in neural activity patterns**

3      Lucy L. W. Owen<sup>1</sup>, Thomas H. Chang<sup>1,2</sup>, and Jeremy R. Manning<sup>1,†</sup>

<sup>1</sup>Department of Psychological and Brain Sciences,  
Dartmouth College, Hanover, NH

<sup>2</sup>Amazon.com, Seattle, WA

†Address correspondence to jeremy.r.manning@dartmouth.edu

4      June 16, 2020

5      **Abstract**

6      Our thoughts arise from coordinated patterns of interactions between brain structures that change with  
7      our ongoing experiences. High-order dynamic correlations in neural activity patterns reflect different  
8      subgraphs of the brain’s connectome that display homologous lower-level dynamic correlations. We tested  
9      the hypothesis that high-level cognition is reflected in high-order dynamic correlations in brain activity  
10     patterns. We developed an approach to estimating high-order dynamic correlations in timeseries data, and  
11     we applied the approach to neuroimaging data collected as human participants either listened to a ten-  
12     minute story, listened to a temporally scrambled version of the story, or underwent a resting state scan. We  
13     trained across-participant pattern classifiers to decode (in held-out data) when in the session each neural  
14     activity snapshot was collected. We found that classifiers trained to decode from high-order dynamic  
15     correlations yielded the best performance on data collected as participants listened to the (unscrambled)  
16     story. By contrast, classifiers trained to decode data from scrambled versions of the story or during  
17     the resting state scan yielded the best performance when they were trained using first-order dynamic  
18     correlations or non-correlational activity patterns. We suggest that as our thoughts become more complex,  
19     they are reflected in higher-order patterns of dynamic network interactions throughout the brain.

20     **Introduction**

21     A central goal in cognitive neuroscience is to elucidate the *neural code*: the mapping between (a) mental  
22     states or cognitive representations and (b) neural activity patterns. One means of testing models of the  
23     neural code is to ask how accurately that model is able to “translate” neural activity patterns into known  
24     (or hypothesized) mental states or cognitive representations (e.g., Haxby et al., 2001; Huth et al., 2016, 2012;  
25     Kamitani & Tong, 2005; Mitchell et al., 2008; Nishimoto et al., 2011; Norman et al., 2006; Pereira et al.,  
26     2018; Tong & Pratte, 2012). Training decoding models on different types of neural features (Fig. 1a) can  
27     also help to elucidate which specific aspects of neural activity patterns are informative about cognition—  
28     and, by extension, which types of neural activity patterns might comprise the neural code. For example,  
29     prior work has used region of interest analyses to estimate the anatomical locations of specific neural  
30     representations (e.g., Etzel et al., 2009), or to compare the relative contributions to the neural code of

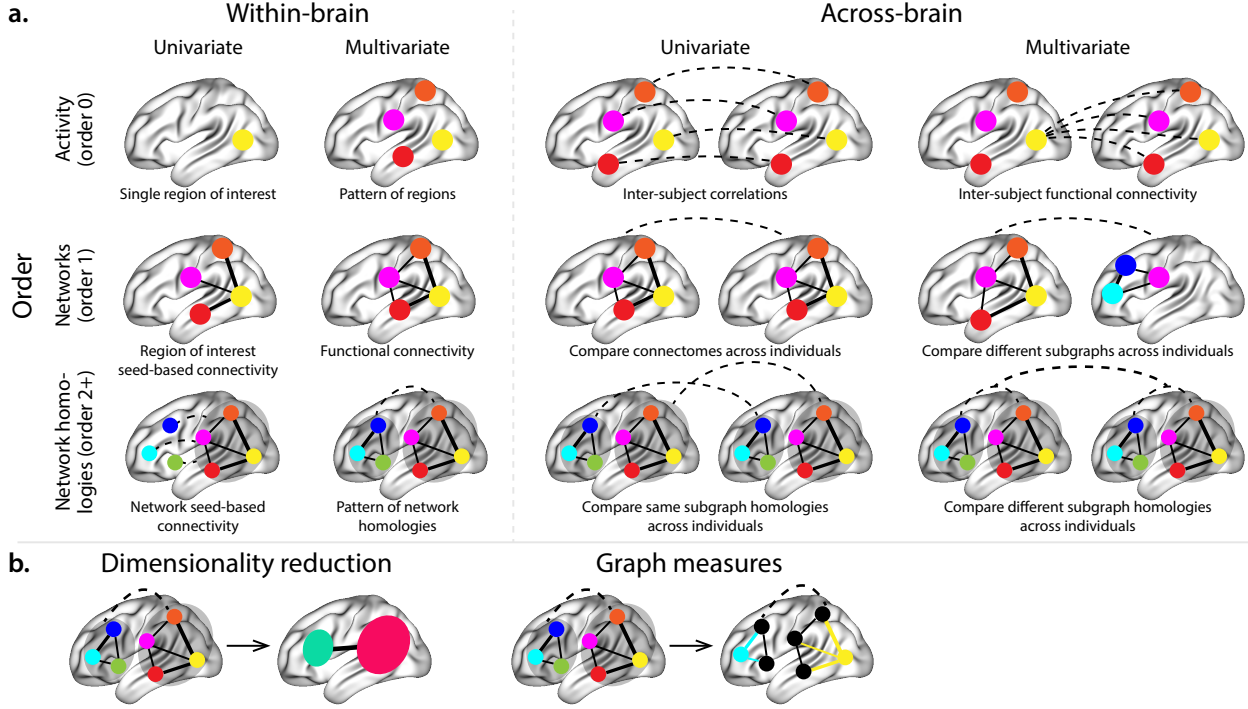


**Figure 1: Neural patterns. a. A space of neural features.** Within-brain analyses are carried out within a single brain, whereas across-brain analyses compare neural patterns across two or more individuals' brains. Univariate analyses characterize the activities of individual units (e.g., nodes, small networks, hierarchies of networks, etc.), whereas multivariate analyses characterize the patterns of activities across units. Order 0 patterns involve individual nodes; order 1 patterns involve node-node interactions; order 2 (and higher) patterns relate to interactions between homologous networks. Each of these patterns may be static (e.g., averaging over time) or dynamic. **b. Summarizing neural patterns.** To efficiently compute with complex neural patterns, it can be useful to characterize the patterns using summary measures. Dimensionality reduction algorithms project the patterns onto lower-dimensional spaces whose dimensions reflect weighted combinations or non-linear transformations of the dimensions in the original space. Graph measures characterize each unit's participation in its associated network.

multivariate activity patterns versus dynamic correlations between neural activity patterns (e.g., Fong et al., 2019; Manning et al., 2018). An emerging theme in this literature is that cognition is mediated by dynamic interactions between brain structures (Bassett et al., 2006; Demertzi et al., 2019; Lurie et al., 2018; Mack et al., 2017; Preti et al., 2017; Solomon et al., 2019; Sporns & Honey, 2006; Turk-Browne, 2013; Zou et al., 2019). Studies of the neural code to date have primarily focused on univariate or multivariate neural patterns (for review see Norman et al., 2006), or (more recently) on patterns of dynamic first-order correlations (i.e., interactions between pairs of brain structures; Demertzi et al., 2019; Fong et al., 2019; Lurie et al., 2018; Manning et al., 2018; Preti et al., 2017; Zou et al., 2019). We wondered what the future of this line of work might hold. For example, is the neural code mediated by higher-order interactions between brain structures (e.g., see Reimann et al., 2017)? Second-order correlations reflect *homologous* patterns of

41 correlation. In other words, if the dynamic patterns of correlations between two regions,  $A$  and  $B$ , are similar  
42 to those between two other regions,  $C$  and  $D$ , this would be reflected in the second-order correlations be-  
43 tween ( $A-B$ ) and ( $C-D$ ). In this way, second-order correlations identify similarities and differences between  
44 subgraphs of the brain’s connectome. Analogously, third-order correlations reflect homologies between  
45 second-order correlations— i.e., homologous patterns of homologous interactions between brain regions.  
46 More generally, higher-order correlations reflect homologies between patterns of lower-order correlations.  
47 We can then ask: which “orders” of interaction are most reflective of high-level cognitive processes?

48 Another central question pertains to the extent to which the neural code is carried by activity patterns  
49 that directly reflect ongoing cognition (e.g., following Haxby et al., 2001; Norman et al., 2006), versus the  
50 dynamic properties of the network structure itself, independent of specific activity patterns in any given  
51 set of regions (e.g., following Bassett et al., 2006). For example, graph measures such as centrality and  
52 degree (Bullmore & Sporns, 2009) may be used to estimate how a given brain structure is “communicating”  
53 with other structures, independently of the specific neural representations carried by those structures.  
54 If one considers a brain region’s position in the network (e.g., its eigenvector centrality) as a dynamic  
55 property, one can compare how the positions of different regions are correlated, and/or how those patterns  
56 of correlations change over time. We can also compute higher-order patterns in these correlations to  
57 characterize homologous subgraphs in the connectome that display similar changes in their constituent  
58 brain structures’ interactions with the rest of the brain.

59 To gain insights into the above aspects of the neural code, we developed a computational framework  
60 for estimating dynamic high-order correlations in timeseries data. This framework provides an important  
61 advance, in that it enables us to examine patterns of higher-order correlations that are computationally  
62 intractable to estimate via conventional methods. Given a multivariate timeseries, our framework provides  
63 timepoint-by-timepoint estimates of the first-order correlations, second-order correlations, and so on. Our  
64 approach combines a kernel-based method for computing dynamic correlations in timeseries data with a di-  
65 mensionality reduction step (Fig. 1b) that projects the resulting dynamic correlations into a low-dimensional  
66 space. We explored two dimensionality reduction approaches: principle components analysis (PCA; Pear-  
67 son, 1901), which preserves an approximately invertible transformation back to the original data (e.g., this  
68 follows related approaches taken by Gonzalez-Castillo et al., 2019; McIntosh & Jirsa, 2019; Toker & Som-  
69 mer, 2019); and a second non-invertible algorithm that explored patterns in eigenvector centrality (Landau,  
70 1895). This latter approach characterizes correlations between each feature dimension’s relative *position* in  
71 the network in favor of the specific activity histories of different features (also see Betzel et al., 2019; Reimann  
72 et al., 2017; Sizemore et al., 2018).

73 We validated our approach using synthetic data where the underlying correlations were known. We

74 then applied our framework to a neuroimaging dataset collected as participants listened to either an audio  
75 recording of a ten-minute story, listened to a temporally scrambled version of the story, or underwent a  
76 resting state scan (Simony et al., 2016). We used a subset of the data to train across-participant classifiers  
77 to decode listening times using a blend of neural features (comprising neural activity patterns, as well as  
78 different orders of dynamic correlations between those patterns that were inferred using our computational  
79 framework). We found that both the PCA-based and eigenvector centrality-based approaches yielded neural  
80 patterns that could be used to decode accurately (i.e., well above chance). Both approaches also yielded  
81 the best decoding accuracy for data collected during (intact) story listening when high-order (PCA: second-  
82 order; eigenvector centrality: fourth-order) dynamic correlation patterns were included as features. When  
83 we trained classifiers on the scrambled stories or resting state data, only lower-order dynamic patterns were  
84 informative to the decoders. Taken together, our results indicate that high-level cognition is supported by  
85 high-order dynamic patterns of communication between brain structures.

## 86 Methods

87 Our general approach to efficiently estimating high-order dynamic correlations comprises four general  
88 steps (Fig. 2). First, we derive a kernel-based approach to computing dynamic pairwise correlations in  
89 a  $T$  (timepoints) by  $K$  (features) multivariate timeseries,  $\mathbf{X}_0$ . This yields a  $T$  by  $O(K^2)$  matrix of dynamic  
90 correlations,  $\mathbf{Y}_1$ , where each row comprises the upper triangle and diagonal of the correlation matrix at  
91 a single timepoint, reshaped into a row vector (this reshaped vector is  $(\frac{K^2-K}{2} + K)$ -dimensional). Second,  
92 we apply a dimensionality reduction step to project the matrix of dynamic correlations back onto a  $K$ -  
93 dimensional space. This yields a  $T$  by  $K$  matrix,  $\mathbf{X}_1$ , that reflects an approximation of the dynamic correlations  
94 reflected in the original data. Third, we use repeated applications of the kernel-based dynamic correlation  
95 step to  $\mathbf{X}_n$  and the dimensionality reduction step to the resulting  $\mathbf{Y}_{n+1}$  to estimate high-order dynamic  
96 correlations. Each application of these steps to a  $T$  by  $K$  time series  $\mathbf{X}_n$  yields a  $T$  by  $K$  matrix,  $\mathbf{X}_{n+1}$ , that  
97 reflects the dynamic correlations between the columns of  $\mathbf{X}_n$ . In this way, we refer to  $n$  as the *order* of the  
98 timeseries, where  $\mathbf{X}_0$  (order 0) denotes the original data and  $\mathbf{X}_n$  denotes (approximated)  $n^{\text{th}}$ -order dynamic  
99 correlations between the columns of  $\mathbf{X}_0$ . Finally, we use a cross-validation-based decoding approach to  
100 evaluate how well information contained in a given order (or weighted mixture of orders) may be used  
101 to decode relevant cognitive states. If including a given  $\mathbf{X}_n$  in the feature set yields higher classification  
102 accuracy on held-out data, we interpret this as evidence that the given cognitive states are reflected in  
103 patterns of  $n^{\text{th}}$ -order correlations. All of the code used to produce the figures and results in this manuscript,  
104 along with links to the corresponding datasets, may be found at [github.com/ContextLab/timecorr-paper](https://github.com/ContextLab/timecorr-paper). In

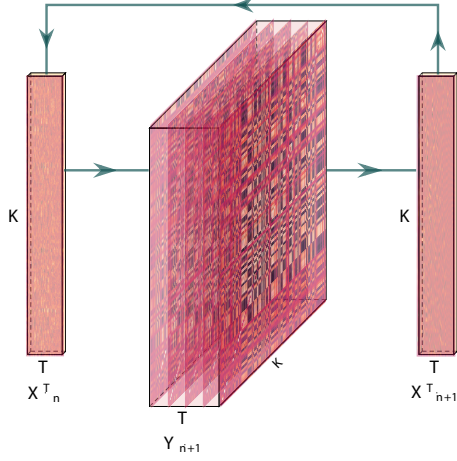


Figure 2: **Estimating dynamic high-order correlations.** Given a  $T$  by  $K$  matrix of multivariate timeseries data,  $\mathbf{X}_n$  (where  $n \in \mathbb{N}, n \geq 0$ ), we use Equation 4 to compute a timeseries of  $K$  by  $K$  correlation matrices,  $\mathbf{Y}_{n+1}$ . We then approximate  $\mathbf{Y}_{n+1}$  with the  $T$  by  $K$  matrix  $\mathbf{X}_{n+1}$ . This process may be repeated to scalably estimate iteratively higher-order correlations in the data. Note that the transposes of  $\mathbf{X}_n$  and  $\mathbf{X}_{n+1}$  are displayed in the figure for compactness.

105 addition, we have released a Python toolbox for computing dynamic high-order correlations in timeseries  
 106 data; our toolbox may be found at [timecorr.readthedocs.io](http://timecorr.readthedocs.io).

## 107 Kernel-based approach for computing dynamic correlations

Given a  $T$  by  $K$  matrix of observations,  $\mathbf{X}$ , we can compute the (static) Pearson's correlation between any pair of columns,  $\mathbf{X}(\cdot, i)$  and  $\mathbf{X}(\cdot, j)$  using (Pearson, 1901):

$$\text{corr}(\mathbf{X}(\cdot, i), \mathbf{X}(\cdot, j)) = \frac{\sum_{t=1}^T (\mathbf{X}(t, i) - \bar{\mathbf{X}}(\cdot, i)) (\mathbf{X}(t, j) - \bar{\mathbf{X}}(\cdot, j))}{\sqrt{\sum_{t=1}^T \sigma_{\mathbf{X}(\cdot, i)}^2 \sigma_{\mathbf{X}(\cdot, j)}^2}}, \text{ where} \quad (1)$$

$$\bar{\mathbf{X}}(\cdot, k) = \frac{1}{T} \sum_{t=1}^T \mathbf{X}(t, k), \text{ and} \quad (2)$$

$$\sigma_{\mathbf{X}(\cdot, k)}^2 = \frac{1}{T} \sum_{t=1}^T (\mathbf{X}(t, k) - \bar{\mathbf{X}}(\cdot, k))^2 \quad (3)$$

108 We can generalize this formula to compute time-varying correlations by incorporating a *kernel function* that  
 109 takes a time  $t$  as input, and returns how much the observed data at each timepoint  $\tau \in [-\infty, \infty]$  contributes  
 110 to the estimated instantaneous correlation at time  $t$  (Fig. 3; also see Allen et al., 2012, for a similar approach).

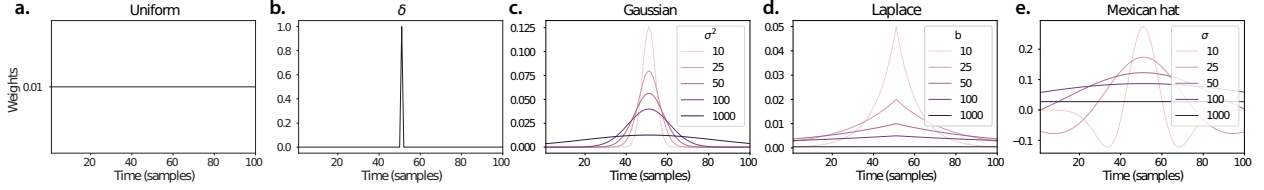


**Figure 3: Examples of kernel functions.** Each panel displays per-timepoint weights for a kernel centered at  $t = 50$ , evaluated at 100 timepoints ( $\tau \in [1, \dots, 100]$ ). **a. Uniform kernel.** The weights are timepoint-invariant; observations at all timepoints are weighted equally, and do not change as a function of  $\tau$ . This is a special case kernel function that reduces dynamic correlations to static correlations. **b. Dirac  $\delta$  kernel.** Only the observation at timepoint  $t$  is given a non-zero weight (of 1). **c. Gaussian kernels.** Each kernel's weights fall off in time according to a Gaussian probability density function centered on time  $t$ . Weights derived using several different example width parameters ( $\sigma^2$ ) are displayed. **d. Laplace kernels.** Each kernel's weights fall off in time according to a Laplace probability density function centered on time  $t$ . Weights derived using several different example width parameters ( $b$ ) are displayed. **e. Mexican hat (Ricker wavelet) kernels.** Each kernel's weights fall off in time according to a Ricker wavelet centered on time  $t$ . This function highlights the *contrasts* between local versus surrounding activity patterns in estimating dynamic correlations. Weights derived using several different example width parameters ( $\sigma$ ) are displayed.

Given a kernel function  $\kappa_t(\cdot)$  for timepoint  $t$ , evaluated at timepoints  $\tau \in [1, \dots, T]$ , we can update the static correlation formula in Equation 1 to estimate the *instantaneous correlation* at timepoint  $t$ :

$$\text{timecorr}_{\kappa_t}(\mathbf{X}(\cdot, i), \mathbf{X}(\cdot, j)) = \frac{\sum_{\tau=1}^T (\mathbf{X}(\tau, i) - \tilde{\mathbf{X}}_{\kappa_t}(\cdot, i))(\mathbf{X}(\tau, j) - \tilde{\mathbf{X}}_{\kappa_t}(\cdot, j))}{\sqrt{\sum_{\tau=1}^T \tilde{\sigma}_{\kappa_t}^2(\mathbf{X}(\cdot, i)) \tilde{\sigma}_{\kappa_t}^2(\mathbf{X}(\cdot, j))}}, \text{ where} \quad (4)$$

$$\tilde{\mathbf{X}}_{\kappa_t}(\cdot, k) = \sum_{\tau=1}^T \kappa_t(\tau) \mathbf{X}(\tau, k), \quad (5)$$

$$\tilde{\sigma}_{\kappa_t}^2(\mathbf{X}(\cdot, k)) = \sum_{\tau=1}^T (\mathbf{X}(\tau, k) - \tilde{\mathbf{X}}_{\kappa_t}(\cdot, k))^2. \quad (6)$$

112 Here  $\text{timecorr}_{\kappa_t}(\mathbf{X}(\cdot, i), \mathbf{X}(\cdot, j))$  reflects the correlation at time  $t$  between columns  $i$  and  $j$  of  $\mathbf{X}$ , estimated using  
 113 the kernel  $\kappa_t$ . We evaluate Equation 4 in turn for each pair of columns in  $\mathbf{X}$  and for kernels centered on each  
 114 timepoint in the timeseries, respectively, to obtain a  $T$  by  $K$  by  $K$  timeseries of dynamic correlations,  $\mathbf{Y}$ . For  
 115 convenience, we then reshape the upper triangles and diagonals of each timepoint's correlation matrix into  
 116 a row vector to obtain an equivalent  $T$  by  $(\frac{K^2-K}{2} + K)$  matrix.

#### 117 Dynamic inter-subject functional connectivity (DISFC)

Equation 4 provides a means of taking a single observation matrix,  $\mathbf{X}_n$  and estimating the dynamic correlations from moment to moment,  $\mathbf{Y}_{n+1}$ . Suppose that one has access to a set of multiple observation matrices that reflect the same phenomenon. For example, one might collect neuroimaging data from several experimental participants, as each participant performs the same task (or sequence of tasks). Let  $\mathbf{X}_n^1, \mathbf{X}_n^2,$

...,  $\mathbf{X}_n^P$  reflect the  $T$  by  $K$  observation matrices ( $n = 0$ ) or reduced correlation matrices ( $n > 0$ ) for each of  $P$  participants in an experiment. We can use *inter-subject functional connectivity* (ISFC; Simony et al., 2016) to compute the stimulus-driven correlations reflected in the multi-participant dataset at a given timepoint  $t$  using:

$$\bar{\mathbf{C}}(t) = M \left( R \left( \frac{1}{2P} \sum_{p=1}^P Z(\mathbf{Y}_{n+1}^p(t))^\top + Z(\mathbf{Y}_{n+1}^p(t)) \right) \right), \quad (7)$$

where  $M$  extracts and vectorizes the upper triangle and diagonal of a symmetric matrix,  $Z$  is the Fisher z-transformation (Zar, 2010):

$$Z(r) = \frac{\log(1+r) - \log(1-r)}{2}, \quad (8)$$

$R$  is the inverse of  $Z$ :

$$R(z) = \frac{\exp(2z-1)}{\exp(2z+1)}, \quad (9)$$

and  $\mathbf{Y}_{n+1}^p(t)$  denotes the correlation matrix at timepoint  $t$  (Eqn. 4) between each column of  $\mathbf{X}_n^p$  and each column of the average  $\mathbf{X}_n$  from all *other* participants,  $\bar{\mathbf{X}}_n^{\setminus p}$ :

$$\bar{\mathbf{X}}_n^{\setminus p} = \frac{1}{P-1} \sum_{q \in \setminus p} \mathbf{X}_n^q, \quad (10)$$

118 where  $\setminus p$  denotes the set of all participants other than participant  $p$ . In this way, the  $T$  by  $\left(\frac{K^2-K}{2} + K\right)$  DISFC  
119 matrix  $\bar{\mathbf{C}}$  provides a time-varying extension of the ISFC approach developed by Simony et al. (2016).

## 120 Low-dimensional representations of dynamic correlations

121 Given a  $T$  by  $\left(\frac{K^2-K}{2} + K\right)$  matrix of  $n^{\text{th}}$ -order dynamic correlations,  $\mathbf{Y}_n$ , we propose two general approaches  
122 to computing a  $T$  by  $K$  low-dimensional representation of those correlations,  $\mathbf{X}_n$ . The first approach uses  
123 dimensionality reduction algorithms to project  $\mathbf{Y}_n$  onto a  $K$ -dimensional space. The second approach uses  
124 graph measures to characterize the relative positions of each feature ( $k \in [1, \dots, K]$ ) in the network defined  
125 by the correlation matrix at each timepoint.

126 **Dimensionality reduction-based approaches to computing  $\mathbf{X}_n$**

127 The modern toolkit of dimensionality reduction algorithms include Principal Components Analysis (PCA;  
128 Pearson, 1901), Probabilistic PCA (PPCA; Tipping & Bishop, 1999), Exploratory Factor Analysis (EFA;  
129 Spearman, 1904), Independent Components Analysis (ICA; Comon et al., 1991; Jutten & Herault, 1991),  $t$ -  
130 Stochastic Neighbor Embedding ( $t$ -SNE; van der Maaten & Hinton, 2008), Uniform Manifold Approximation  
131 and Projection (UMAP; ?), non-negative matrix factorization (NMF; Lee & Seung, 1999), Topographic Factor  
132 Analysis (TFA; Manning et al., 2014), Hierarchical Topographic Factor analysis (HTFA; Manning et al., 2018),  
133 Topographic Latent Source Analysis (TLSA; Gershman et al., 2011), dictionary learning (J. Mairal et al., 2009;  
134 J. B. Mairal et al., 2009), and deep auto-encoders (Hinton & Salakhutdinov, 2006), among others. While  
135 complete characterizations of each of these algorithms is beyond the scope of the present manuscript, the  
136 general intuition driving these approaches is to compute the  $T$  by  $K$  matrix,  $\mathbf{X}$ , that is closest to the original  
137  $T$  by  $J$  matrix,  $\mathbf{Y}$ , where (typically)  $K \ll J$ . The different approaches place different constraints on what  
138 properties  $\mathbf{X}$  must satisfy and which aspects of the data are compared (and how) in order to optimize how  
139 well  $\mathbf{X}$  approximates  $\mathbf{Y}$ .

140 Applying dimensionality reduction algorithms to  $\mathbf{Y}$  yields an  $\mathbf{X}$  whose columns reflect weighted combi-  
141 nations (or nonlinear transformations) of the original columns of  $\mathbf{Y}$ . This has two main consequences. First,  
142 with each repeated dimensionality reduction, the resulting  $\mathbf{X}_n$  has lower and lower fidelity (with respect to  
143 what the “true”  $\mathbf{Y}_n$  might have looked like without using dimensionality reduction to maintain scalability).  
144 In other words, computing  $\mathbf{X}_n$  is a lossy operation. Second, whereas each column of  $\mathbf{Y}_n$  may be mapped  
145 directly onto specific pairs of columns of  $\mathbf{X}_{n-1}$ , the columns of  $\mathbf{X}_n$  reflect weighted combinations and/or  
146 nonlinear transformations of the columns of  $\mathbf{Y}_n$ . Many dimensionality reduction algorithms are invertible  
147 (or approximately invertible). However, attempting to map a given  $\mathbf{X}_n$  back onto the original feature space  
148 of  $\mathbf{X}_0$  will usually require  $O(TK^{2n})$  space and therefore becomes intractable as  $n$  or  $K$  grow large.

149 **Graph measure approaches to computing  $\mathbf{X}_n$**

150 The above dimensionality reduction approaches to approximating a given  $\mathbf{Y}_n$  with a lower-dimensional  
151  $\mathbf{X}_n$  preserve a (potentially recombined and transformed) mapping back to the original data in  $\mathbf{X}_0$ . We also  
152 explore graph measures that instead characterize each feature’s relative *position* in the broader network of  
153 interactions and connections. To illustrate the distinction between the two general approaches we explore,  
154 suppose a network comprises nodes  $A$ ,  $B$ , and  $C$ . If  $A$  and  $B$  exhibit uncorrelated activity patterns, the  
155 functional connection (correlation) between them will be (by definition) close to 0. However, if  $A$  and  $B$   
156 each interact with  $C$  in similar ways, we might attempt to capture those similarities using a measure that

157 reflects how  $A$  and  $B$  interact with *other* members of the network.

158 In general, graph measures take as input a matrix of interactions (e.g., using the above notation, a  $K$   
159 by  $K$  correlation matrix or binarized correlation matrix reconstituted from a single timepoint's row of  $\mathbf{Y}$ ),  
160 and return as output a set of  $K$  measures describing how each node (feature) sits within that correlation  
161 matrix with respect to the rest of the population. Widely used measures include betweenness centrality (the  
162 proportion of shortest paths between each pair of nodes in the population that involves the given node  
163 in question; e.g., Barthélemy, 2004; Freeman, 1977; Geisberger et al., 2008; Newman, 2005; Opsahl et al.,  
164 2010); diversity and dissimilarity (characterizations of how differently connected a given node is from others  
165 in the population; e.g., Lin, 2009; Rao, 1982; Ricotta & Szeidl, 2006); eigenvector centrality and pagerank  
166 centrality (measures of how influential a given node is within the broader network; e.g., Bonacich, 2007;  
167 Halu et al., 2013; Lohmann et al., 2010; Newman, 2008); transfer entropy and flow coefficients (a measure of  
168 how much information is flowing from a given node to other nodes in the network; e.g., Honey et al., 2007;  
169 Schreiber, 2000);  $k$ -coreness centrality (a measure of the connectivity of a node within its local subgraph; e.g.,  
170 Alvarez-Hamelin et al., 2005; Christakis & Fowler, 2010); within-module degree (a measure of how many  
171 connections a node has to its close neighbors in the network; e.g., Rubinov & Sporns, 2010); participation  
172 coefficient (a measure of the diversity of a node's connections to different subgraphs in the network; e.g.,  
173 Rubinov & Sporns, 2010); and subgraph centrality (a measure of a node's participation in all of the network's  
174 subgraphs; e.g., Estrada & Rodríguez-Velázquez, 2005); among others.

175 For a given graph measure,  $\eta : \mathbb{R}^{K \times K} \rightarrow \mathbb{R}^K$ , we can use  $\eta$  to transform each row of  $\mathbf{Y}_n$  in a way that  
176 characterizes the corresponding graph properties of each column. This results in a new  $T$  by  $K$  matrix,  
177  $\mathbf{X}_n$ , that reflects how the features reflected in the columns of  $\mathbf{X}_{n-1}$  participate in the network during each  
178 timepoint (row).

## 179 **Dynamic higher-order correlations**

180 Because  $\mathbf{X}_n$  has the same shape as the original data  $\mathbf{X}_0$ , approximating  $\mathbf{Y}_n$  with a lower-dimensional  $\mathbf{X}_n$   
181 enables us to estimate high-order dynamic correlations in a scalable way. Given a  $T$  by  $K$  input matrix, the  
182 output of Equation 4 requires  $O(TK^2)$  space to store. Repeated applications of Equation 4 (i.e., computing  
183 dynamic correlations between the columns of the outputted dynamic correlation matrix) each require  
184 exponentially more space; in general the  $n^{\text{th}}$ -order dynamic correlations of a  $T$  by  $K$  timeseries occupies  
185  $O(TK^{2n})$  space. However, when we approximate or summarize the output of Equation 4 with a  $T$  by  $K$  matrix  
186 (as described above), it becomes feasible to compute even very high-order correlations in high-dimensional  
187 data. Specifically, approximating the  $n^{\text{th}}$ -order dynamic correlations of a  $T$  by  $K$  timeseries requires only

188  $O(TK^2)$  additional space– the same as would be required to compute first-order dynamic correlations. In  
189 other words, the space required to store  $n + 1$  multivariate timeseries reflecting up to  $n^{\text{th}}$  order correlations  
190 in the original data scales linearly with  $n$  using our approach (Fig. 2).

191 **Data**

192 We examined two types of data: synthetic data and human functional neuroimaging data. We constructed  
193 and leveraged the synthetic data to evaluate our general approach (for a related validation approach see  
194 Thompson et al., 2018). Specifically, we tested how well Equation 4 could be used to recover known dynamic  
195 correlations using different choices of kernel ( $\kappa$ ; Fig. 3), for each of several synthetic datasets that exhibited  
196 different temporal properties. We also used this synthetic data to simulate higher-order correlations and  
197 tested how well Equation 4 could recover these correlations using the best kernel from the previous synthetic  
198 data analysis. We applied our approach to a functional neuroimaging dataset to test the hypothesis that  
199 ongoing cognitive processing is reflected in high-order dynamic correlations. We used an across-participant  
200 classification test to estimate whether dynamic correlations of different orders contain information about  
201 which timepoint in a story participants were listening to.

202 **Synthetic data**

203 We constructed a total of 40 different multivariate timeseries, collectively reflecting a total of 4 qualitatively  
204 different patterns of dynamic correlations (i.e., 10 datasets reflecting each type of dynamic pattern). Each  
205 timeseries comprised 50 features (dimensions) that varied over 300 timepoints. The observations at each  
206 timepoint were drawn from a zero-mean multivariate Gaussian distribution with a covariance matrix  
207 defined for each timepoint as described below. We drew the observations at each timepoint independently  
208 from the draws at all other timepoints; in other words, for each observation  $s_t \sim \mathcal{N}(\mathbf{0}, \Sigma_t)$  at timepoint  $t$ ,  
209  $p(s_t) = p(s_t | s_{\setminus t})$ .

**Constant.** We generated data with stable underlying correlations to evaluate how Equation 4 characterized correlation “dynamics” when the ground truth correlations were static. We constructed 10 multivariate timeseries whose observations were each drawn from a single (stable) Gaussian distribution. For each dataset (indexed by  $m$ ), we constructed a random covariance matrix,  $\Sigma_m$ :

$$\mathbf{C}(i, j) \sim \mathcal{N}(0, 1) \quad (11)$$

$$\Sigma_m = \mathbf{C}\mathbf{C}^\top, \text{ where} \quad (12)$$

210     $i, j \in [1, 2, \dots, 50]$ . In other words, all of the observations (for each of the 300 timepoints) within each dataset  
 211    were drawn from a multivariate Gaussian distribution with the same covariance matrix, and the 10 datasets  
 212    each used a different covariance matrix.

213    **Random.** We generated a second set of 10 synthetic datasets whose observations at each timepoint were  
 214    drawn from a Gaussian distribution with a new randomly constructed (using Eqn. 12) covariance matrix.  
 215    Because each timepoint's covariance matrix was drawn independently from the covariance matrices for all  
 216    other timepoints, these datasets provided a test of reconstruction accuracy in the absence of any meaningful  
 217    underlying temporal structure in the dynamic correlations underlying the data.

**Ramping.** We generated a third set of 10 synthetic datasets whose underlying correlations changed gradually over time. For each dataset, we constructed two *anchor* covariance matrices using Equation 12,  $\Sigma_{\text{start}}$  and  $\Sigma_{\text{end}}$ . For each of the 300 timepoints in each dataset, we drew the observations from a multivariate Gaussian distribution whose covariance matrix at each timepoint  $t \in [0, \dots, 299]$  was given by

$$\Sigma_t = \left(1 - \frac{t}{299}\right)\Sigma_{\text{start}} + \frac{t}{299}\Sigma_{\text{end}}. \quad (13)$$

218    The gradually changing correlations underlying these datasets allow us to evaluate the recovery of dynamic  
 219    correlations when each timepoint's correlation matrix is unique (as in the random datasets), but where the  
 220    correlation dynamics are structured and exhibit first-order autocorrelations (as in the constant datasets).

221    **Event.** We generated a fourth set of 10 synthetic datasets whose underlying correlation matrices exhibited  
 222    prolonged intervals of stability, interspersed with abrupt changes. For each dataset, we used Equation 12  
 223    to generate 5 random covariance matrices. We constructed a timeseries where each set of 60 consecutive  
 224    samples was drawn from a Gaussian with the same covariance matrix. These datasets were intended to  
 225    simulate a system that undergoes occasional abrupt state changes.

## 226    Simulated higher-order correlations

227    We simulated first and second order correlations reflecting the 4 qualitatively different patterns of synthetic  
 228    dynamic correlations. We repeated the processes 10 times for each order and for each of the 4 dynamic  
 229    pattern (Constant, Random, Ramping, and Event) explored in *Synthetic data*. First, we generated a timeseries  
 230    of correlations which comprised 50 features (dimensions) that varied over 300 timepoints using 1 of the 4  
 231    *Synthetic data* dynamic patterns. To calculate the next increasing order of correlations,  $Y_{n+1,t}$ , we multiplied  
 232    the vectorized correlation matrix by its transpose, for each timepoint:

$$Y_{n=1,t} = \text{vec}(\Sigma_t) \cdot \text{vec}(\Sigma_t)^\top \quad (14)$$

$$Y_{n+1,t} = \text{vec}(Y_{n,t}) \cdot \text{vec}(Y_{n,t})^\top \quad (15)$$

We repeated this processes for the number of desired orders ( $N$ ) to generate a timeseries of  $N^{\text{th}}$  correlation matrices. Then, observations were drawn at each timepoint from a  $Y_{N-1,t}$ -mean multivariate Gaussian distribution with a covariance matrix defined as  $Y_{N+1,t}$  and the resultant vector was reshaped to the matrix the size of  $Y_{N-1,t}$ :

$$\hat{Y}_{N-1,t} \sim \text{vec}(\mathcal{N}(Y_{n,t}, Y_{N,t}))^{-1} \quad (16)$$

This process was then repeated for all decreasing orders, in which observations werre drawn at each timepoint from a  $Y_{n,t}$ -mean multivariate Gaussian distribution, but the covariance matrix is defined at the previously estimated reshaped matrix  $\hat{Y}_{n,t}$ :

$$\hat{Y}_{n,t} \sim \text{vec}(\mathcal{N}(Y_{n,t}, \hat{Y}_{n+1,t}))^{-1} \quad (17)$$

<sup>233</sup> We repeat this process until  $n = 1$ , then we drew observations at each timepoint from a zero-mean multi-  
<sup>234</sup> variate Gaussian distribution with a covariance matrix defined for each timepoint as described below:

$$s_t \sim \mathcal{N}(\mathbf{0}, \hat{Y}_{n=1,t}) \quad (18)$$

<sup>235</sup> For our specific analyses the resulting synthetic timeseries comprised 50 features and 300 timepoints.  
<sup>236</sup> We then used this synthetic data to test how well Equation 4 could recover the simulated first and second  
<sup>237</sup> order correlations. To mitigate temporal blur in estimating each timeseries of dynamic correlations, we  
<sup>238</sup> used a Dirac  $\delta$  function kernel (which places all of its mass over a single timepoint) Fig. 3b) to compute  
<sup>239</sup> each lower-order correlation and then used a Laplace kernel with a width of 20 to compute  $\mathbf{X}_{n,t}$ , applying  
<sup>240</sup> temporal blur at just the last step. Then, for each timepoint, we correlated the simulated correlation matix,  
<sup>241</sup>  $Y_{n,t}$  with the Equation 4 estimated correllation matric,  $\mathbf{X}_{n,t}$ .

242 **Functional neuroimaging data collected during story listening**

243 We examined an fMRI dataset collected by Simony et al. (2016) that the authors have made publicly available  
244 at [arks.princeton.edu/ark:/88435/dsp015d86p269k](https://arks.princeton.edu/ark:/88435/dsp015d86p269k). The dataset comprises neuroimaging data collected as  
245 participants listened to an audio recording of a story (intact condition; 36 participants), listened to temporally  
246 scrambled recordings of the same story (17 participants in the paragraph-scrambled condition listened to  
247 the paragraphs in a randomized order and 36 in the word-scrambled condition listened to the words in a  
248 randomized order), or lay resting with their eyes open in the scanner (rest condition; 36 participants). Full  
249 neuroimaging details may be found in the original paper for which the data were collected (Simony et al.,  
250 2016).

251 **Hierarchical topographic factor analysis (HTFA).** Following our prior related work, we used HTFA (Manning et al., 2018) to derive a compact representation of the neuroimaging data. In brief, this approach approximates the timeseries of voxel activations (44,415 voxels) using a much smaller number of radial basis  
252 function (RBF) nodes (in this case, 700 nodes, as determined by an optimization procedure described by  
253 Manning et al., 2018). This provides a convenient representation for examining full-brain network dynamics.  
254 All of the analyses we carried out on the neuroimaging dataset were performed in this lower-dimensional  
255 space. In other words, each participant's data matrix,  $X_0$ , was a number-of-timepoints by 700 matrix of  
256 HTFA-derived factor weights (where the row and column labels were matched across participants). Code  
257 for carrying out HTFA on fMRI data may be found as part of the BrainIAK toolbox (Capota et al., 2017),  
258 which may be downloaded at [brainiak.org](http://brainiak.org).

261 **Temporal decoding**

262 We sought to identify neural patterns that reflected participants' ongoing cognitive processing of incoming  
263 stimulus information. As reviewed by Simony et al. (2016), one way of homing in on these stimulus-  
264 driven neural patterns is to compare activity patterns across individuals (e.g., using ISFC analyses). In  
265 particular, neural patterns will be similar across individuals to the extent that the neural patterns under  
266 consideration are stimulus-driven, and to the extent that the corresponding cognitive representations are  
267 reflected in similar spatial patterns across people. Following this logic, we used an across-participant  
268 temporal decoding test developed by Manning et al. (2018) to assess the degree to which different neural  
269 patterns reflected ongoing stimulus-driven cognitive processing across people. The approach entails using  
270 a subset of the data to train a classifier to decode stimulus timepoints (i.e., moments in the story participants  
271 listened to) from neural patterns. We use decoding (forward inference) accuracy on held-out data, from held-

272 out participants, as a proxy for the extent to which the inputted neural patterns reflected stimulus-driven  
273 cognitive processing in a similar way across individuals.

274 **Forward inference and decoding accuracy**

275 We used an across-participant correlation-based classifier to decode which stimulus timepoint matched  
276 each timepoint's neural pattern. We first divided the participants into two groups: a template group,  
277  $\mathcal{G}_{\text{template}}$ , and a to-be-decoded group,  $\mathcal{G}_{\text{decode}}$ . We used Equation 7 to compute a DISFC matrix for each  
278 group ( $\bar{\mathbf{C}}_{\text{template}}$  and  $\bar{\mathbf{C}}_{\text{decode}}$ , respectively). We then correlated the rows of  $\bar{\mathbf{C}}_{\text{template}}$  and  $\bar{\mathbf{C}}_{\text{decode}}$  to form a  
279 number-of-timepoints by number-of-timepoints decoding matrix,  $\Lambda$ . In this way, the rows of  $\Lambda$  reflected  
280 timepoints from the template group, while the columns reflected timepoints from the to-be-decoded group.  
281 We used  $\Lambda$  to assign temporal labels to each row  $\bar{\mathbf{C}}_{\text{decode}}$  using the row of  $\bar{\mathbf{C}}_{\text{template}}$  with which it was most  
282 highly correlated. We then repeated this decoding procedure, but using  $\mathcal{G}_{\text{decode}}$  as the template group  
283 and  $\mathcal{G}_{\text{template}}$  as the to-be-decoded group. Given the true timepoint labels (for each group), we defined the  
284 *decoding accuracy* as the average proportion of correctly decoded timepoints, across both groups. We defined  
285 the *relative decoding accuracy* as the difference between the decoding accuracy and chance accuracy (i.e.,  $\frac{1}{T}$ ).

286 **Feature weighting and testing**

287 We sought to examine which types of neural features (i.e., activations, first-order dynamic correlations, and  
288 higher-order dynamic correlations) were informative to the temporal decoders. Using the notation above,  
289 these features correspond to  $\mathbf{X}_0, \mathbf{X}_1, \mathbf{X}_2, \mathbf{X}_3$ , and so on.

290 One challenge to fairly evaluating high-order correlations is that if the kernel used in Equation 4 is  
291 wider than a single timepoint, each repeated application of the equation will result in further temporal  
292 blur. Because our primary assessment metric is temporal decoding accuracy, this unfairly biases against  
293 detecting meaningful signal in higher-order correlations (relative to lower-order correlations). We attempted  
294 to mitigate temporal blur in estimating each  $\mathbf{X}_n$  by using a Dirac  $\delta$  function kernel (which places all of its  
295 mass over a single timepoint; Fig. 3b) to compute each lower-order correlation ( $\mathbf{X}_1, \mathbf{X}_2, \dots, \mathbf{X}_{n-1}$ ). We then  
296 used a new (potentially wider, as described below) kernel to compute  $\mathbf{X}_n$  from  $\mathbf{X}_{n-1}$ . In this way, temporal  
297 blurring was applied only in the last step of computing  $\mathbf{X}_n$ . We note that, because each  $\mathbf{X}_n$  is a low-  
298 dimensional representation of the corresponding  $\mathbf{Y}_n$ , the higher-order correlations we estimated reflect true  
299 correlations in the data with lower-fidelity than estimates of lower-order correlations. Therefore, even  
300 after correcting for temporal blurring, our approach is still biased against finding meaningful signal in  
301 higher-order correlations.

302 After computing each  $\mathbf{X}_1, \mathbf{X}_2, \dots, \mathbf{X}_{n-1}$  for each participant, we divided participants into two equally sized  
303 groups ( $\pm 1$  for odd numbers of participants):  $\mathcal{G}_{\text{train}}$  and  $\mathcal{G}_{\text{test}}$ . We then further subdivided  $\mathcal{G}_{\text{train}}$  into  $\mathcal{G}_{\text{train}_1}$   
304 and  $\mathcal{G}_{\text{train}_2}$ . We then computed  $\Lambda$  (temporal correlation) matrices for each type of neural feature, using  $\mathcal{G}_{\text{train}_1}$   
305 and  $\mathcal{G}_{\text{train}_2}$ . This resulted in  $n + 1$   $\Lambda$  matrices (one for the original timeseries of neural activations, and one  
306 for each of  $n$  orders of dynamic correlations). Our objective was to find a set of weights for each of these  
307  $\Lambda$  matrices such that the weighted average of the  $n + 1$  matrices yielded the highest decoding accuracy.  
308 We used quasi-Newton gradient ascent (Nocedal & Wright, 2006), using decoding accuracy (for  $\mathcal{G}_{\text{train}_1}$  and  
309  $\mathcal{G}_{\text{train}_2}$ ) as the objective function to be maximized, to find an optimal set of training data-derived weights,  
310  $\phi_{0,1,\dots,n}$ , where  $\sum_{i=0}^n \phi_i = 1$  and where  $\phi_i \geq 0 \forall i \in [0, 1, \dots, n]$ .

311 After estimating an optimal set of weights, we computed a new set of  $n + 1$   $\Lambda$  matrices correlating the  
312 DISFC patterns from  $\mathcal{G}_{\text{train}}$  and  $\mathcal{G}_{\text{test}}$  at each timepoint. We use the resulting decoding accuracy of  $\mathcal{G}_{\text{test}}$   
313 timepoints (using the weights in  $\phi_{0,1,\dots,n}$  to average the  $\Lambda$  matrices) to estimate how informative the set of  
314 neural features containing up to  $n^{\text{th}}$  order correlations were.

315 We used a permutation-based procedure to form stable estimates of decoding accuracy for each set of  
316 neural features. In particular, we computed the decoding accuracy for each of 10 random group assignments  
317 of  $\mathcal{G}_{\text{train}}$  and  $\mathcal{G}_{\text{test}}$ . We report the mean accuracy (along with 95% confidence intervals) for each set of neural  
318 features.

### 319 Identifying robust decoding results

320 The temporal decoding procedure we use to estimate which neural features support ongoing cognitive  
321 processing is governed by several parameters. In particular, Equation 4 requires defining a kernel function,  
322 which can take on different shapes and widths. For a fixed set of neural features, each of these parameters  
323 can yield different decoding accuracies. Further, the best decoding accuracy for a given timepoint may be  
324 reliably achieved by one set of parameters, whereas the best decoding accuracy for another timepoint might  
325 be reliably achieved by a different set of parameters, and the best decoding accuracy across *all* timepoints  
326 might be reliably achieved by still another different set of parameters. Rather than attempting to maximize  
327 decoding accuracy, we sought to discover the trends in the data that were robust to classifier parameters  
328 choices. Specifically, we sought to characterize how decoding accuracy varied (under different experimental  
329 conditions) as a function of which neural features were considered.

330 To identify decoding results that were robust to specific classifier parameter choices, we repeated our  
331 decoding analyses after substituting into Equation 4 each of a variety of kernel shapes and widths. We  
332 examined Gaussian (Fig. 3c), Laplace (Fig. 3d), and Mexican Hat (Fig. 3e) kernels, each with widths of 5, 10,

333 20, and 50 samples. We then report the average decoding accuracies across all of these parameter choices.  
334 This enabled us to (partially) factor out performance characteristics that were parameter-dependent, within  
335 the set of parameters we examined.

336 **Reverse inference**

337 The dynamic patterns we examined comprise high-dimensional correlation patterns at each timepoint. To  
338 help interpret the resulting patterns in the context of other studies, we created summary maps by computing  
339 the across-timepoint average pairwise correlations at each order of analysis (first order, second order, etc.).  
340 We selected the 10 strongest (absolute value) correlations at each order. Each correlation is between the  
341 dynamic activity patterns (or patterns of dynamic high-order correlations) measured at two RBF nodes  
342 (see *Hierarchical Topographic Factor Analysis*). Therefore, the 10 strongest correlations involved up to 20 RBF  
343 nodes. Each RBF defines a spatial function whose activations range from 0 to 1. We constructed a map  
344 of RBF components that denoted the endpoints of the 10 strongest correlations (we set each RBF to have a  
345 maximum value of 1). We then carried out a meta analysis using Neurosynth (Rubin et al., 2017) to identify  
346 the 10 terms most commonly associated with the given map. This resulted in a set of 10 terms associated  
347 with the average dynamic correlation patterns at each order.

348 **Results**

349 We sought to understand whether high-level cognition is reflected in dynamic patterns of high-order  
350 correlations. To that end, we developed a computational framework for estimating the dynamics of stimulus-  
351 driven high-order correlations in multivariate timeseries data (see *Dynamic inter-subject functional connectivity*  
352 (*DISFC*) and *Dynamic higher-order correlations*). We evaluated the efficacy of this framework at recovering  
353 known patterns in several synthetic datasets (see *Synthetic data*). We then applied the framework to a public  
354 fMRI dataset collected as participants listened to an auditorily presented story, listened to a temporally  
355 scrambled version of the story, or underwent a resting state scan (see *Functional neuroimaging data collected*  
356 *during story listening*). We used the relative decoding accuracies of classifiers trained on different sets of  
357 neural features to estimate which types of features reflected ongoing cognitive processing.

358 **Recovering known dynamic correlations from synthetic data**

359 We generated synthetic datasets that differed in how the underlying correlations changed over time. For  
360 each dataset, we applied Equation 4 with a variety of kernel shapes and widths. We assessed how well

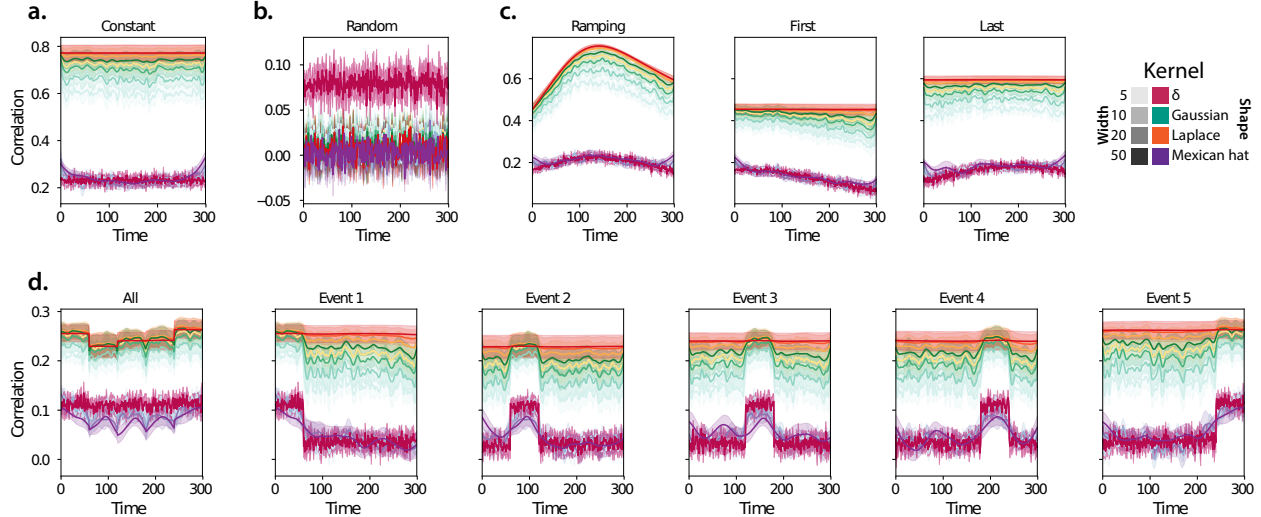


**Figure 4: Recovering known dynamic correlations from synthetic data.** Each panel displays the average correlations between the vectorized upper triangles of the recovered correlation matrix at each timepoint and either the true underlying correlation at each timepoint or a reference correlation matrix. (The averages are taken across 10 different randomly generated synthetic datasets of the given category.) Error ribbons denote 95% confidence intervals (taken across datasets). Different colors denote different kernel shapes, and the shading within each color family denotes the kernel width parameter. For a complete description of each synthetic dataset, see *Synthetic data*. **a. Constant correlations.** These datasets have a stable (unchanging) underlying correlation matrix. **b. Random correlations.** These datasets are generated using a new independently drawn correlation matrix at each new timepoint. **c. Ramping correlations.** These datasets are generated by smoothly varying the underlying correlations between the randomly drawn correlation matrices at the first and last timepoints. The left panel displays the correlations between the recovered dynamic correlations and the underlying ground truth correlations. The middle panel compares the recovered correlations with the *first* timepoint's correlation matrix. The right panel compares the recovered correlations with the *last* timepoint's correlation matrix. **d. Event-based correlations.** These datasets are each generated using five randomly drawn correlation matrices that each remain stable for a fifth of the total timecourse. The left panel displays the correlations between the recovered dynamic correlations and the underlying ground truth correlations. The right panels compare the recovered correlations with the correlation matrices unique to each event.

361 the true underlying correlations at each timepoint matched the recovered correlations (Fig. 4). For every  
 362 kernel and dataset we tested, our approach recovered the correlation dynamics we embedded into the data.  
 363 However, the quality of these recoveries varied across different synthetic datasets in a kernel-dependent  
 364 way.

365 In general, wide monotonic kernel shapes (Laplace, Gaussian), and wider kernels (within a shape),  
 366 performed best when the correlations varied gradually from moment-to-moment (Figs. 4a, c, and d). In the  
 367 extreme, as the rate of change in correlations approaches 0 (Fig. 4a), an infinitely wide kernel would exactly  
 368 recover the Pearson's correlation (e.g., compare Eqns. 1 and 4).

369 When the correlation dynamics were unstructured in time (Fig. 4b), a Dirac  $\delta$  kernel (infinitely narrow)  
 370 performed best. This is because, when every timepoint's correlations are independent of the correlations at

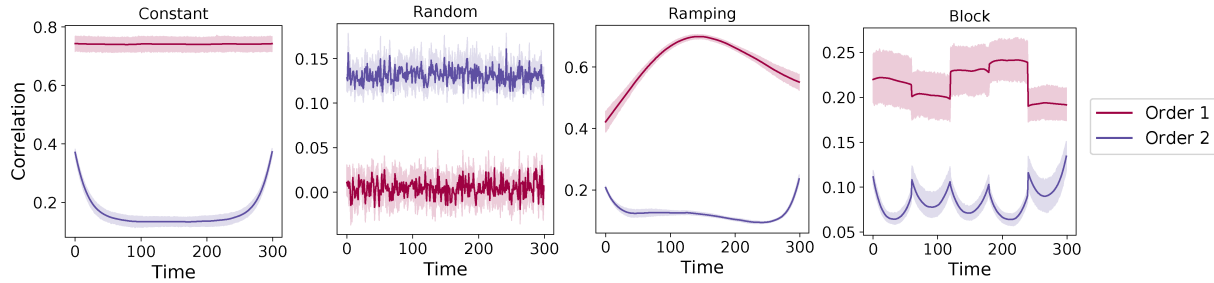


Figure 5: **Recovery of simulated first and second order dynamic correlations.** Each panel displays the average correlations between the vectorized upper triangles of the recovered correlation matrix and the simulated correlation matrix at each timepoint and for each synthetic dataset. (The averages are taken across 10 different randomly generated synthetic datasets of the given category.) Error ribbons denote 95% confidence intervals (taken across datasets). For a complete description of each synthetic dataset, see *Synthetic data*. **a. Constant correlations.** These first and second order dynamic correlation were simulated from datasets have a stable (unchanging) underlying correlation matrix. **b. Random correlations.** These first and second order dynamic correlation were simulated from datasets are generated using a new independently drawn correlation matrix at each new timepoint. **c. Ramping correlations.** These first and second order dynamic correlation were simulated from datasets are generated by smoothly varying the underlying correlations between the randomly drawn correlation matrices at the first and last timepoints and displays the correlations between the recovered dynamic correlations and the simulalted correlation first and second order correlation matrices. **d. Event-based correlations.** These first and second order dynamic correlation were simulated from datasets are each generated using five randomly drawn correlation matrices that each remain stable for a fifth of the total timecourse.

371 every other timepoint, averaging data over time dilutes the available signal. Following a similar pattern,  
 372 holding kernel shape fixed, narrower kernel parameters better recovered randomly varying correlations.

### 373 Recovering known higher-order dynamic correlations from synthetic data

374 We generated a synthetic timeseries from simulated first and second order dynamic correlation matrices that  
 375 differed in how the underlying correlations changed over time. For each dataset, we applied Equation 4 with  
 376 a Laplace kernel with a width of 20. We assessed how well the recovered correlations matched simulated  
 377 first and second order correlations. (Fig. 5). For every dataset we tested, our approach recovered the  
 378 correlation dynamics we embedded into the data. However, the quality of these recoveries varied across  
 379 different synthetic datasets.

### 380 Cognitively relevant dynamic high-order correlations in fMRI data

381 We used across-participant temporal decoders to identify cognitively relevant neural patterns in fMRI data  
 382 (see *Forward inference and decoding accuracy*). The dataset we examined (collected by Simony et al., 2016)  
 383 comprised four experimental conditions that exposed participants to stimuli that varied systematically in  
 384 how cognitively engaging they were. The *intact* experimental condition had participants listen to an audio

recording of a 10-minute story. The *paragraph*-scrambled experimental condition had participants listen to a temporally scrambled version of the story, where the paragraphs occurred out of order (but where the same total set of paragraphs were presented over the full listening interval). All participants in this condition experienced the scrambled paragraphs in the same order. The *word*-scrambled experimental condition had participants listen to a temporally scrambled version of the story where the words in the story occurred in a random order. All participants in the word condition experienced the scrambled words in the same order. Finally, in a *rest* experimental condition, participants lay in the scanner with no overt stimulus, with their eyes open (blinking as needed). This dataset provided a convenient means of testing our hypothesis that different levels of cognitive processing and engagement are reflected in different orders of brain activity dynamics.

In brief, we computed timeseries of dynamic high-order correlations that were similar across participants in each of two randomly assigned groups: a training group and a test group. We then trained classifiers on the training group's data to match each sample from the test group with a stimulus timepoint. Each classifier comprised a weighted blend of neural patterns that reflected up to  $n^{\text{th}}$ -order dynamic correlations (see *Feature weighting and testing*). We repeated this process for  $n \in \{0, 1, 2, \dots, 10\}$ . Our examinations of synthetic data suggested that none of the kernels we examined were "universal" in the sense of optimally recovering underlying correlations regardless of the temporal structure of those correlations. We found a similar pattern in the (real) fMRI data, whereby different kernels yielded different decoding accuracies, but no single kernel emerged as the clear "best." In our analyses of neural data, we therefore averaged our decoding results over a variety of kernel shapes and widths in order to identify results that were robust to specific kernel parameters (see *Identifying robust decoding results*).

Our approach to estimating dynamic high-order correlations entails mapping the high-dimensional feature space of correlations (a  $T$  by  $O(K^2)$  matrix) onto a lower-dimensional  $T$  by  $K$  matrix. We carried out two sets of analyses that differed in how this mapping was computed. The first set of analyses used PCA to find a low-dimensional embedding of the original dynamic correlation matrices (Fig. 6a,b). The second set of analyses characterized correlations in dynamics of each feature's eigenvector centrality, but did not preserve the underlying activity dynamics (Fig. 6c,d).

Both sets of temporal decoding analyses yielded qualitatively similar results for the auditory (non-rest) conditions of the experiment (Fig. 6: pink, green, and teal lines; Fig. 7: three leftmost columns). The highest decoding accuracy for participants who listened to the intact (unscrambled) story was achieved using high-order dynamic correlations (PCA: second-order; eigenvector-centrality: fourth-order). Scrambled versions of the story were best decoded by lower-order correlations (PCA/paragraph: first-order; PCA/word: order zero; eigenvector centrality/paragraph: order zero; eigenvector centrality/word: order zero). The two sets

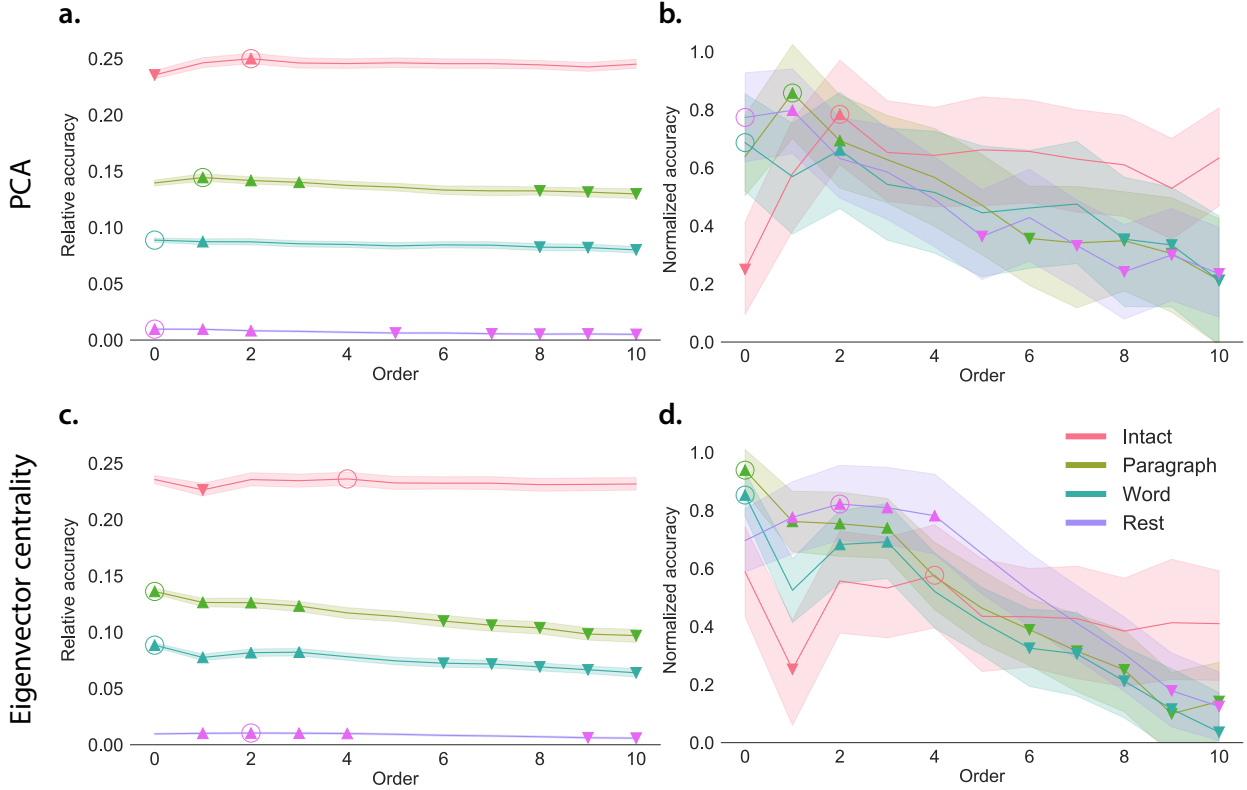


**Figure 6: Across-participant timepoint decoding accuracy varies with correlation order and cognitive engagement.** **a. Decoding accuracy as a function of order: PCA.** Order (*x*-axis) refers to the maximum order of dynamic correlations that were available to the classifiers (see *Feature weighting and testing*). The reported across-participant decoding accuracies are averaged over all kernel shapes and widths (see *Identifying robust decoding results*). The *y*-values are displayed relative to chance accuracy (intact:  $\frac{1}{300}$ ; paragraph:  $\frac{1}{272}$ ; word:  $\frac{1}{300}$ ; rest:  $\frac{1}{400}$ ). The error ribbons denote 95% confidence intervals across cross-validation folds (i.e., random assignments of participants to the training and test sets). The colors denote the experimental condition. Arrows denote sets of features that yielded reliably higher (upwards facing) or lower (downward facing) decoding accuracy than the mean of all other features (via a two-tailed test, thresholded at  $p < 0.05$ ). Figure 7 displays additional comparisons between the decoding accuracies achieved using different sets of neural features. The circled values represent the maximum decoding accuracy within each experimental condition. **b. Normalized timepoint decoding accuracy as a function of order: PCA.** This panel displays the same results as Panel a, but here each curve has been normalized to have a maximum value of 1 and a minimum value of 0 (including the upper and lower bounds of the respective 95% confidence intervals). Panels a and b used PCA to project each high-dimensional pattern of dynamic correlations onto a lower-dimensional space. **c. Timepoint decoding accuracy as a function of order: eigenvector centrality.** This panel is in the same format as Panel a, but here eigenvector centrality has been used to project the high-dimensional patterns of dynamic correlations onto a lower-dimensional space. **d. Normalized timepoint decoding accuracy as a function of order: eigenvector centrality.** This panel is in the same format as Panel b, but here eigenvector centrality has been used to project the high-dimensional patterns of dynamic correlations onto a lower-dimensional space.

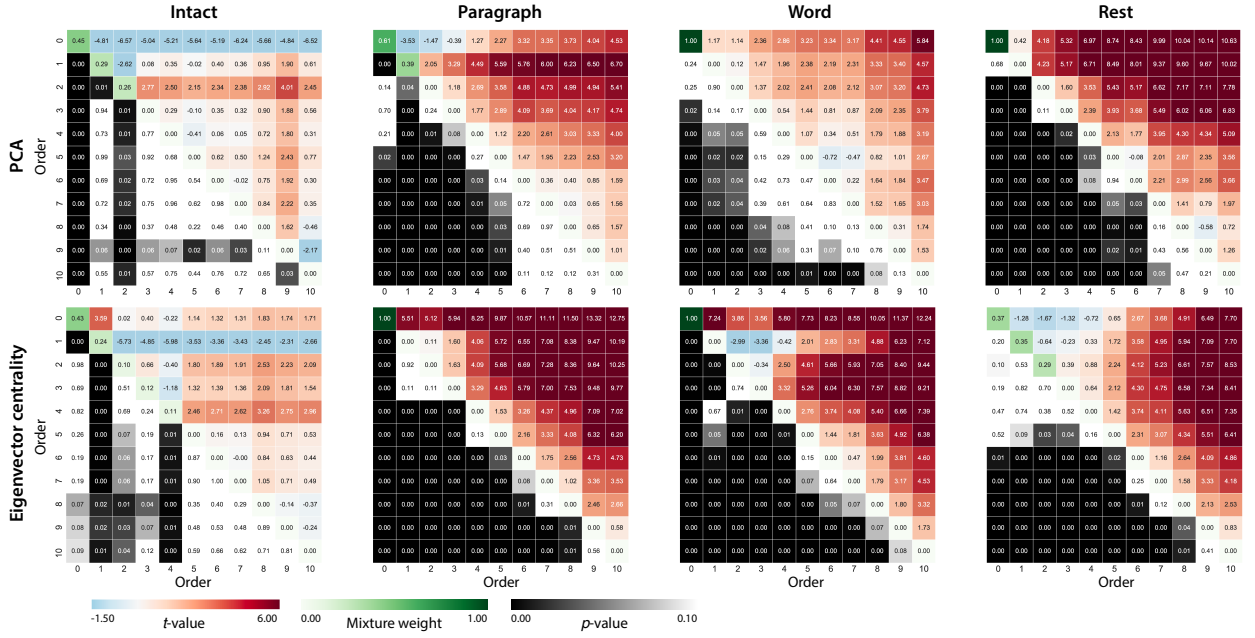


**Figure 7: Statistical summary of decoding accuracies for different neural features.** Each column displays decoding results for one experimental condition (intact, paragraph, word, and rest). We considered dynamic activity patterns (order 0) and dynamic correlations at different orders (order  $> 0$ ). We used two-tailed  $t$ -tests to compare the distributions of decoding accuracies obtained using each pair of features. The distributions for each feature reflect the set of average decoding accuracies (across all kernel parameters), obtained for each random assignment of training and test groups. In the upper triangles of each map, warmer colors (positive  $t$ -values) indicate that the neural feature indicated in the given row yielded higher accuracy than the feature indicated in the given column. Cooler colors (negative  $t$ -values) indicate that the feature in the given row yielded lower decoding accuracy than the feature in the given column. The lower triangles of each map denote the corresponding  $p$ -values for the  $t$ -tests. The diagonal entries display the relative average optimized weight given to each type of feature, in a decoder that included all feature types (see *Feature weighting and testing*).

418 of analyses yielded different decoding results on resting state data (Fig. 6: purple lines; Fig. 7: rightmost  
419 column). We note that while the resting state times could be decoded reliably, the accuracies were only very  
420 slightly above chance. We speculate that the decoders might have picked up on attentional drift, boredom,  
421 or tiredness; we hypothesize that these all increased throughout the resting state scan. The decoders might  
422 be picking up on aspects of these loosely defined cognitive states that are common across individuals. The  
423 PCA-based approach achieved the highest resting state decoding accuracy using order zero features (non-  
424 correlational, activation-based), whereas the eigenvector centrality-based approach achieved the highest  
425 resting state decoding accuracy using second-order correlations. Taken together, these analyses indicate  
426 that high-level cognitive processing (while listening to the intact story) is reflected in the dynamics of high-  
427 order correlations in brain activity, whereas lower-level cognitive processing (while listening to scrambled  
428 versions of the story that lack rich meaning) is reflected in the dynamics of lower-order correlations and  
429 non-correlational activity dynamics. Further, these patterns are associated both with the underlying activity  
430 patterns (characterized using PCA) and also with the changing relative positions that different brain areas  
431 occupy in their associated networks (characterized using eigenvector centrality).

432 Having established that patterns of high-order correlations are informative to decoders, we next won-  
433 dered which specific networks of brain regions contributed most to these patterns. As a representative  
434 example, we selected the kernel parameters that yielded decoding accuracies that best matched the average  
435 accuracies across all of the kernel parameters we examined. Using Figure 6c as a template, the best-matching  
436 kernel was a Laplace kernel with a width of 50 (Fig. 3d). We used this kernel to compute a single  $K$  by  $K$   
437  $n^{\text{th}}$ -order DISFC matrix for each experimental condition. We then used Neurosynth (Rubin et al., 2017) to  
438 compute the terms most highly associated with the most strongly correlated pairs of regions in each of these  
439 matrices (Fig. 8; see *Reverse inference*).

440 For all of the story listening conditions (intact, paragraph, and word), we found that first- and second-  
441 order correlations were most strongly associated with auditory and speech processing areas. During  
442 intact story listening, third-order correlations reflected integration with visual areas, and fourth-order  
443 correlations reflected integration with areas associated with high-level cognition and cognitive control,  
444 such as the ventrolateral prefrontal cortex. However, during listening to temporally scrambled stories,  
445 these higher-order correlations instead involved interactions with additional regions associated with speech  
446 and semantic processing. By contrast, we found a much different set of patterns in the resting state data.  
447 First-order resting state correlations were most strongly associated with regions involved in counting and  
448 numerical understanding. Second-order resting state correlations were strongest in visual areas; third-order  
449 correlations were strongest in task-positive areas; and fourth-order correlations were strongest in regions  
450 associated with autobiographical and episodic memory. We carried out analogous analyses to create maps

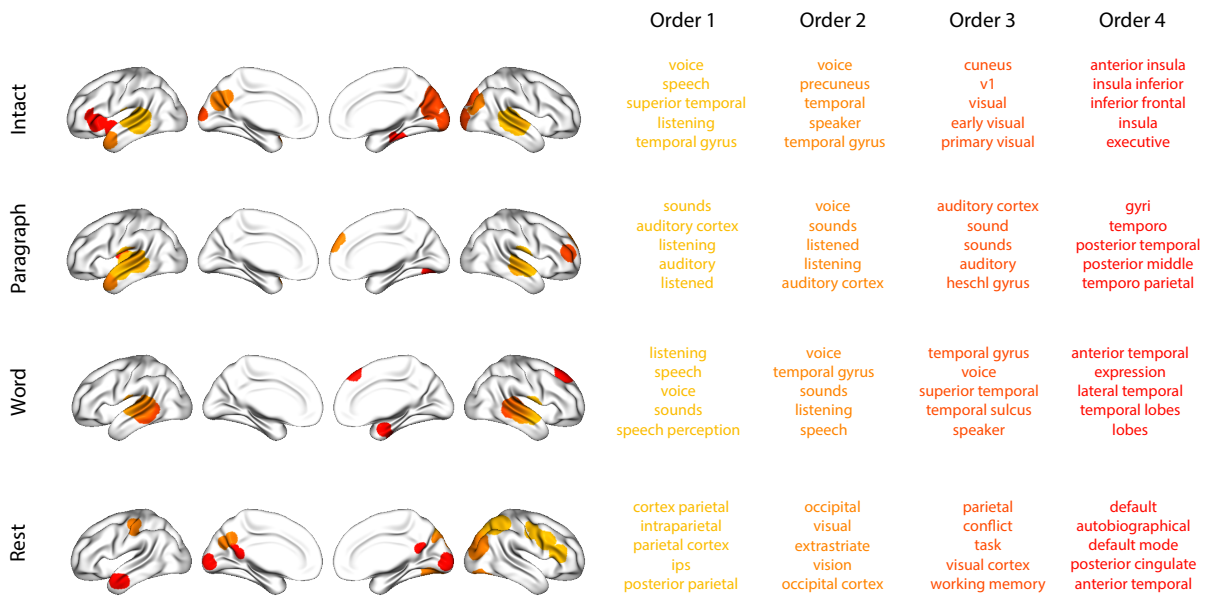


**Figure 8: Top terms associated with the endpoints of the strongest correlations.** Each color corresponds to one order of inter-subject functional correlations. To calculate the dynamic correlations, eigenvector centrality has been used to project the high-dimensional patterns of dynamic correlations onto a lower-dimensional space at each previous order, which allows us to map the brain regions at each order by retaining the features of the original space. The inflated brain plots display the locations of the endpoints of the 10 strongest (absolute value) correlations at each order, thresholded at 0.999, and projected onto the cortical surface (Combrisson et al., 2019). The lists of terms on the right display the top five Neurosynth terms (Rubin et al., 2017) decoded from the corresponding brain maps for each order. Each row displays data from a different experimental condition. Additional maps and their corresponding Neurosynth terms may be found in the *Supplementary materials* (intact: Fig. S1; paragraph: Fig. S2; word: Fig. S3; rest: Fig. S4).

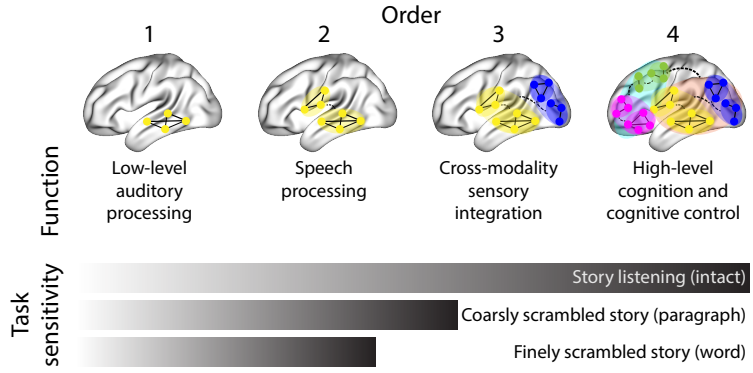


**Figure 9: Proposed high-order network dynamics underlying high-level cognition during story listening.** Schematic depicts higher orders of network interactions supporting higher-level aspects of cognitive processing. When tasks evoke richer, deeper, and/or higher-level processing, this is reflected in higher-order network interactions.

451 (and decode the top associated Neurosynth terms) for up to fifteenth-order correlations (Figs. S1, S2, S3, and  
 452 S4). Of note, examining fifteenth-order correlations between 700 nodes using conventional methods would  
 453 have required storing roughly  $\frac{700^{2 \times 15}}{2} \approx 1.13 \times 10^{85}$  floating point numbers—assuming single-precision (32  
 454 bits each), this would require roughly 32 times as many bits as there are molecules in the known universe!  
 455 Although these fifteenth-order correlations do appear (visually) to have some well-formed structure, we  
 456 provide this latter example primarily as a demonstration of the efficiency and scalability of our approach.

## 457 Discussion

458 We tested the hypothesis that high-level cognition is reflected in high-order brain network dynamics (e.g.,  
 459 see Reimann et al., 2017; Solomon et al., 2019). We examined high-order network dynamics in functional  
 460 neuroimaging data collected during a story listening experiment. When participants listened to an auditory  
 461 recording of the story, participants exhibited similar high-order brain network dynamics. By contrast,  
 462 when participants instead listened to temporally scrambled recordings of the story, only lower-order brain  
 463 network dynamics were similar across participants. Our results indicate that higher orders of network  
 464 interactions support higher-level aspects of cognitive processing (Fig. 9).

465 The notion that cognition is reflected in (and possibly mediated by) patterns of first-order network  
 466 dynamics has been suggested by or proposed in myriad empirical studies and reviews (e.g., Chang &  
 467 Glover, 2010; Demertzi et al., 2019; Fong et al., 2019; Gonzalez-Castillo et al., 2019; Liégeois et al., 2019; Lurie  
 468 et al., 2018; Park et al., 2018; Preti et al., 2017; Roy et al., 2019; Turk-Browne, 2013; Zou et al., 2019). Our study  
 469 extends this line of work by finding cognitively relevant *higher-order* network dynamics that reflect ongoing  
 470 cognition. Our findings complement other work that uses graph theory and topology to characterize how

471 brain networks reconfigure during cognition (e.g., Bassett et al., 2006; Betzel et al., 2019; McIntosh & Jirsa,  
472 2019; Reimann et al., 2017; Sizemore et al., 2018; Toker & Sommer, 2019; Zheng et al., 2019).

473 An open question not addressed by our study pertains to how different structures integrate incoming  
474 information with different time constants. For example, one line of work suggests that the cortical surface  
475 comprises a structured map such that nearby brain structures process incoming information at similar  
476 timescales. Low-level sensory areas integrate information relatively quickly, whereas higher-level regions  
477 integrate information relatively slowly (Baldassano et al., 2017; Chien & Honey, 2019; Hasson et al., 2015,  
478 2008; Honey et al., 2012; Lerner et al., 2014, 2011). Other related work in human and mouse brains indicates  
479 that the temporal response profile of a given brain structure may relate to how strongly connected that  
480 structure is with other brain areas (Fallon et al., 2019). Further study is needed to understand the role of  
481 temporal integration at different scales of network interaction, and across different anatomical structures.  
482 Importantly, our analyses do no speak to the physiological basis of higher-order dynamics, and could reflect  
483 nonlinearities, chaotic patterns, non-stationarities, or multistability, etc. However, our decoding analyses  
484 do indicate that higher-order dynamics are consistent across individuals, and therefore unlikely to be driven  
485 by non-stimulus-driven dynamics which are unlikely to be similar across individuals.

486 Another potential limitation of our approach relates to recent work suggesting that the brain undergoes  
487 rapid state changes, for example across event boundaries (e.g., Baldassano et al., 2017). Shappell et al.  
488 (2019) used hidden semi-Markov models to estimate state-specific network dynamics (also see Vidaurre et  
489 al., 2018). Our general approach might be extended by considering putative state transitions. For example,  
490 rather than weighting all timepoints using a similar kernel (Eqn. 4), the kernel function could adapt on a  
491 timepoint-by-timepoint basis such that only timepoints determined to be in the same “state” were given  
492 non-zero weight.

493 Identifying high-order network dynamics associated with high-level cognition required several impor-  
494 tant methods advances. First, we used kernel-based dynamic correlations to extended the notion of (static)  
495 inter-subject functional connectivity (Simony et al., 2016) to a dynamic measure of inter-subject functional  
496 connectivity (DISFC) that does not rely on sliding windows, and that may be computed at individual  
497 timepoints. This allowed us to precisely characterize stimulus-evoked network dynamics that were similar  
498 across individuals. Second, we developed a computational framework for efficiently and scalably estimat-  
499 ing high-order dynamic correlations. Our approach uses dimensionality reduction algorithms and graph  
500 measures to obtain low-dimensional embeddings of patterns of network dynamics. Third, we developed  
501 an analysis framework for identifying robust decoding results by carrying out our analyses using a range  
502 of parameter values and then identifying which results were robust to specific parameter choices.

503 **Concluding remarks**

504 The complex hierarchy of dynamic interactions that underlie our thoughts is perhaps the greatest mystery in  
505 modern science. Methods for characterizing the dynamics of high-order correlations in neural data provide  
506 a window into the neural basis of cognition. By showing that high-level cognition is reflected in high-order  
507 network dynamics, we have elucidated the next step on the path towards understanding the neural basis  
508 of cognition.

509 **Acknowledgements**

510 We acknowledge discussions with Luke Chang, Vassiki Chauhan, Hany Farid, Paxton Fitzpatrick, Andrew  
511 Heusser, Eshin Jolly, Aaron Lee, Qiang Liu, Matthijs van der Meer, Judith Mildner, Gina Notaro, Stephen  
512 Satterthwaite, Emily Whitaker, Weizhen Xie, and Kirsten Ziman. Our work was supported in part by NSF  
513 EPSCoR Award Number 1632738 to J.R.M. and by a sub-award of DARPA RAM Cooperative Agreement  
514 N66001-14-2-4-032 to J.R.M. The content is solely the responsibility of the authors and does not necessarily  
515 represent the official views of our supporting organizations.

516 **Author contributions**

517 Concept: J.R.M. Implementation: T.H.C., L.L.W.O., and J.R.M. Analyses: L.L.W.O. and J.R.M. Writing:  
518 L.L.W.O. and J.R.M.

519 **References**

- 520 Allen, E. A., Damaraju, E., Plis, S. M., Erhardt, E. B., Eichele, T., & Calhoun, V. D. (2012). Tracking  
521 whole-brain connectivity dynamics in the resting state. *Cerebral Cortex*, 24(3), 663–676.
- 522 Alvarez-Hamelin, I., Dall'Asta, L., Barrat, A., & Vespignani, A. (2005). *k*-corr decomposition: a tool for the  
523 visualiztion of large scale networks. *arXiv*, cs/0504107v2.
- 524 Baldassano, C., Chen, J., Zadbood, A., Pillow, J. W., Hasson, U., & Norman, K. A. (2017). Discovering event  
525 structure in continuous narrative perception and memory. *Neuron*, 95(3), 709–721.
- 526 Barthélémy, M. (2004). Betweenness centrality in large complex networks. *European Physical Journal B*, 38,  
527 163–168.

- 528 Bassett, D., Meyer-Lindenberg, A., Achard, S., Duke, T., & Bullmore, E. (2006, December). Adaptive  
529 reconfiguration of fractal small-world human brain functional networks. *Proceedings of the National  
530 Academy of Sciences, USA*, 103(51), 19518–23.
- 531 Betzel, R. F., Byrge, L., Esfahlani, F. Z., & Kennedy, D. P. (2019). Temporal fluctuations in the brain's modular  
532 architecture during movie-watching. *bioRxiv*, doi.org/10.1101/750919.
- 533 Bonacich, P. (2007). Some unique properties of eigenvector centrality. *Social Networks*, 29(4), 555–564.
- 534 Bullmore, E., & Sporns, O. (2009). Complex brain networks: graph theoretical analysis of structural and  
535 functional systems. *Nature Reviews Neuroscience*, 10(3), 186–198.
- 536 Capota, M., Turek, J., Chen, P.-H., Zhu, X., Manning, J. R., Sundaram, N., . . . Shin, Y. S. (2017). *Brain imaging  
537 analysis kit*. Retrieved from <https://doi.org/10.5281/zenodo.59780>
- 538 Chang, C., & Glover, G. H. (2010). Time-frequency dynamics of resting-state brain connectivity measured  
539 with fMRI. *NeuroImage*, 50, 81–98.
- 540 Chien, H.-Y. S., & Honey, C. J. (2019). Constructing and forgetting temporal context in the human cerebral  
541 cortex. *bioRxiv*, doi.org/10.1101/761593.
- 542 Christakis, N. A., & Fowler, J. H. (2010). Social network sensors for early detection of contagious outbreaks.  
543 *PLoS One*, 5(9), e12948.
- 544 Combrisson, E., Vallat, R., O'Reilly, C., Jas, M., Pascarella, A., l Saive, A., . . . Jerbi, K. (2019). Visbrain: a  
545 multi-purpose GPU-accelerated open-source suite for multimodal brain data visualization. *Frontiers in  
546 Neuroinformatics*, 13(14), 1–14.
- 547 Comon, P., Jutten, C., & Herault, J. (1991). Blind separation of sources, part II: Problems statement. *Signal  
548 Processing*, 24(1), 11 - 20.
- 549 Demertzi, A., Tagliazucchi, E., Dehaene, S., Deco, G., Barttfeld, P., Raimondo, F., . . . Sitt, J. D. (2019). Human  
550 consciousness is supported by dynamic complex patterns of brain signal coordination. *Science Advances*,  
551 5(2), eaat7603.
- 552 Estrada, E., & Rodríguez-Velázquez, J. A. (2005). Subgraph centrality in complex networks. *Physical Review  
553 E*, 71(5), 056103.
- 554 Etzel, J. A., Gazzola, V., & Keysers, C. (2009). An introduction to anatomical ROI-based fMRI classification.  
555 *Brain Research*, 1281, 114–125.

- 556 Fallon, J., Ward, P., Parkes, L., Oldham, S., Arnatkevičiūtė, A., Fornito, A., & Fulcher, B. D. (2019).  
557 Timescales of spontaneous activity fluctuations relate to structural connectivity in the brain. *bioRxiv*,  
558 doi.org/10.1101/655050.
- 559 Fong, A. H. C., Yoo, K., Rosenberg, M. D., Zhang, S., Li, C.-S. R., Scheinost, D., ... Chun, M. M. (2019).  
560 Dynamic functional connectivity during task performance and rest predicts individual differences in  
561 attention across studies. *NeuroImage*, 188, 14–25.
- 562 Freeman, L. C. (1977). A set of measures of centrality based on betweenness. *Sociometry*, 40(1), 35–41.
- 563 Geisberger, R., Sanders, P., & Schultes, D. (2008). Better approximation of betweenness centrality. *Proceedings*  
564 *of the meeting on Algorithm Engineering and Experiments*, 90–100.
- 565 Gershman, S., Blei, D., Pereira, F., & Norman, K. (2011). A topographic latent source model for fMRI data.  
566 *NeuroImage*, 57, 89–100.
- 567 Gonzalez-Castillo, J., Caballero-Gaudes, C., Topolski, N., Handwerker, D. A., Pereira, F., & Bandettini, P. A.  
568 (2019). Imaging the spontaneous flow of thought: distinct periods of cognition contribute to dynamic  
569 functional connectivity during rest. *NeuroImage*, 202(116129).
- 570 Halu, A., Mondragón, R. J., Panzarasa, P., & Bianconi, G. (2013). Multiplex PageRank. *PLoS One*, 8(10),  
571 e78293.
- 572 Hasson, U., Chen, J., & Honey, C. J. (2015). Hierarchical process memory: memory as an integral component  
573 of information processing. *Trends in Cognitive Science*, 19(6), 304–315.
- 574 Hasson, U., Yang, E., Vallines, I., Heeger, D. J., & Rubin, N. (2008). A hierarchy of temporal receptive windows  
575 in human cortex. *Journal of Neuroscience*, 28(10), 2539–2550. doi: 10.1523/JNEUROSCI.5487-07.2008
- 576 Haxby, J. V., Gobbini, M. I., Furey, M. L., Ishai, A., Schouten, J. L., & Pietrini, P. (2001). Distributed and  
577 overlapping representations of faces and objects in ventral temporal cortex. *Science*, 293, 2425–2430.
- 578 Hinton, G. E., & Salakhutdinov, R. R. (2006). Reducing the dimensionality of data with neural networks.  
579 *Science*, 313(5786), 504–507.
- 580 Honey, C. J., Kötter, R., Breakspear, M., & Sporns, O. (2007). Network structure of cerebral cortex shapes  
581 functional connectivity on multiple time scales. *Proceedings of the National Academy of Science USA*, 104(24),  
582 10240–10245.

- 583 Honey, C. J., Thesen, T., Donner, T. H., Silbert, L. J., Carlson, C. E., Devinsky, O., ... Hasson, U. (2012). Slow  
584 cortical dynamics and the accumulation of information over long timescales. *Neuron*, 76, 423-434. doi:  
585 10.1016/j.neuron.2012.08.011
- 586 Huth, A. G., de Heer, W. A., Griffiths, T. L., Theunissen, F. E., & Gallant, J. L. (2016). Natural speech reveals  
587 the semantic maps that tile human cerebral cortex. *Nature*, 532, 453–458.
- 588 Huth, A. G., Nisimoto, S., Vu, A. T., & Gallant, J. L. (2012). A continuous semantic space describes  
589 the representation of thousands of object and action categories across the human brain. *Neuron*, 76(6),  
590 1210-1224.
- 591 Jutten, C., & Herault, J. (1991). Blind separation of sources, part I: An adaptive algorithm based on  
592 neuromimetic architecture. *Signal Processing*, 24(1), 1–10.
- 593 Kamitani, Y., & Tong, F. (2005). Decoding the visual and subjective contents of the human brain. *Nature*  
594 *Neuroscience*, 8, 679–685.
- 595 Landau, E. (1895). Zur relativen Wertbemessung der Turnierresultate. *Deutsches Wochenschach*, 11, 366–369.
- 596 Lee, D. D., & Seung, H. S. (1999). Learning the parts of objects by non-negative matrix factorization. *Nature*,  
597 401, 788–791.
- 598 Lerner, Y., Honey, C. J., Katkov, M., & Hasson, U. (2014). Temporal scaling of neural responses to compressed  
599 and dilated natural speech. *Journal of Neurophysiology*, 111, 2433–2444.
- 600 Lerner, Y., Honey, C. J., Silbert, L. J., & Hasson, U. (2011). Topographic mapping of a hierarchy of  
601 temporal receptive windows using a narrated story. *Journal of Neuroscience*, 31(8), 2906-2915. doi: 10.1523/  
602 JNEUROSCI.3684-10.2011
- 603 Liégeois, R., Li, J., Kong, R., Orban, C., De Ville, D. V., Ge, T., ... Yeo, B. T. T. (2019). Resting brain  
604 dynamics at different timescales capture distinct aspects of human behavior. *Nature Communications*,  
605 10(2317), doi.org/10.1038/s41467-019-10317-7.
- 606 Lin, J. (2009). Divergence measures based on the Shannon entropy. *IEEE Transactions on Information Theory*,  
607 37(1), 145–151.
- 608 Lohmann, G., Margulies, D. S., Horstmann, A., Pleger, B., Lepsien, J., Goldhahn, D., ... Turner, R. (2010).  
609 Eigenvector centrality mapping for analyzing connectivity patterns in fMRI data of the human brain.  
610 *PLoS One*, 5(4), e10232.

- 611 Lurie, D., Kessler, D., Bassett, D., Betzel, R., Breakspear, M., Keilholz, S., ... Calhoun, V. (2018). On the  
612 nature of time-varying functional connectivity in resting fMRI. *PsyArXiv*, doi.org/10.31234/osf.io/xtzre.
- 613 Mack, M. L., Preston, A. R., & Love, B. C. (2017). Medial prefrontal cortex compresses concept representations  
614 through learning. *bioRxiv*, doi.org/10.1101/178145.
- 615 Mairal, J., Ponce, J., Sapiro, G., Zisserman, A., & Bach, F. R. (2009). Supervised dictionary learning. *Advances*  
616 in *Neural Information Processing Systems*, 1033–1040.
- 617 Mairal, J. B., Bach, F., Ponce, J., & Sapiro, G. (2009). Online dictionary learning for sparse coding. *Proceedings*  
618 of the 26th annual international conference on machine learning, 689–696.
- 619 Manning, J. R., Ranganath, R., Norman, K. A., & Blei, D. M. (2014). Topographic factor analysis: a Bayesian  
620 model for inferring brain networks from neural data. *PLoS One*, 9(5), e94914.
- 621 Manning, J. R., Zhu, X., Willke, T. L., Ranganath, R., Stachenfeld, K., Hasson, U., ... Norman, K. A. (2018).  
622 A probabilistic approach to discovering dynamic full-brain functional connectivity patterns. *NeuroImage*,  
623 180, 243–252.
- 624 McIntosh, A. R., & Jirsa, V. K. (2019). The hidden repertoire of brain dynamics and dysfunction. *Network*  
625 *Neuroscience*, doi.org/10.1162/netn\_a\_00107.
- 626 Mitchell, T., Shinkareva, S., Carlson, A., Chang, K., Malave, V., Mason, R., & Just, M. (2008). Predicting  
627 human brain activity associated with the meanings of nouns. *Science*, 320(5880), 1191.
- 628 Newman, M. E. J. (2005). A measure of betweenness centrality based on random walks. *Social Networks*, 27,  
629 39–54.
- 630 Newman, M. E. J. (2008). The mathematics of networks. *The New Palgrave Encyclopedia of Economics*, 2, 1–12.
- 631 Nishimoto, S., Vu, A., Naselaris, T., Benjamini, Y., Yu, B., & Gallant, J. (2011). Reconstructing visual  
632 experience from brain activity evoked by natural movies. *Current Biology*, 21, 1 - 6.
- 633 Nocedal, J., & Wright, S. J. (2006). *Numerical optimization*. New York: Springer.
- 634 Norman, K. A., Newman, E., Detre, G., & Polyn, S. M. (2006). How inhibitory oscillations can train neural  
635 networks and punish competitors. *Neural Computation*, 18, 1577–1610.
- 636 Opsahl, T., Agneessens, F., & Skvoretz, J. (2010). Node centrality in weighted networks: generalizing degree  
637 and shortest paths. *Social Networks*, 32, 245–251.

- 638 Park, H.-J., Friston, K. J., Pae, C., Park, B., & Razi, A. (2018). Dynamic effective connectivity in resting state  
639 fMRI. *NeuroImage*, 180, 594–608.
- 640 Pearson, K. (1901). On lines and planes of closest fit to systems of points in space. *The London, Edinburgh,  
641 and Dublin Philosophical Magazine and Journal of Science*, 2, 559–572.
- 642 Pereira, F., Lou, B., Pritchett, B., Ritter, S., Gershman, S. J., Kanwisher, N., ... Fedorenko, E. (2018). Toward  
643 a universal decoder of linguistic meaning from brain activation. *Nature Communications*, 9(963), 1–13.
- 644 Preti, M. G., Bolton, T. A. W., & Van De Ville, D. (2017). The dynamic functional connectome: state-of-the-art  
645 and perspectives. *NeuroImage*, 160, 41–54.
- 646 Rao, C. R. (1982). Diversity and dissimilarity coefficients: a unified approach. *Theoretical Population Biology*,  
647 21(1), 24–43.
- 648 Reimann, M. W., Nolte, M., Scolamiero, M., Turner, K., Perin, R., Chindemi, G., ... Markram, H. (2017).  
649 Cliques of neurons bound into cavities provide a missing link between structure and function. *Frontiers  
650 in Computational Neuroscience*, 11(48), 1–16.
- 651 Ricotta, C., & Szeidl, L. (2006). Towards a unifying approach to diversity measures: Bridging the gap  
652 between the Shannon entropy and Rao's quadratic index. *Theoretical Population Biology*, 70(3), 237–243.
- 653 Roy, D. S., Park, Y.-G., Ogawa, S. K., Cho, J. H., Choi, H., Kamensky, L., ... Tonegawa, S. (2019). Brain-  
654 wide mapping of contextual fear memory engram ensembles supports the dispersed engram complex  
655 hypothesis. *bioRxiv*, doi.org/10.1101/668483.
- 656 Rubin, T. N., Kyoejo, O., Gorgolewski, K. J., Jones, M. N., Poldrack, R. A., & Yarkoni, T. (2017). Decoding  
657 brain activity using a large-scale probabilistic functional-anatomical atlas of human cognition. *PLoS  
658 Computational Biology*, 13(10), e1005649.
- 659 Rubinov, M., & Sporns, O. (2010). Complex network measures of brain connectivity: uses and interpreta-  
660 tions. *NeuroImage*, 52, 1059–1069.
- 661 Schreiber, T. (2000). Measuring information transfer. *Physical Review Letters*, 85(2), 461–464.
- 662 Shappell, H., Caffo, B. S., Pekar, J. J., & Lindquist, M. A. (2019). Improved state change estimation in  
663 dynamic functional connectivity using hidden semi-Markov models. *NeuroImage*, 191, 243–257.
- 664 Simony, E., Honey, C. J., Chen, J., & Hasson, U. (2016). Uncovering stimulus-locked network dynamics  
665 during narrative comprehension. *Nature Communications*, 7(12141), 1–13.

- 666 Sizemore, A. E., Giusti, C., Kahn, A., Vettel, J. M., Betzel, R. F., & Bassett, D. S. (2018). Cliques and cavities  
667 in the human connectome. *Journal of Computational Neuroscience*, 44(1), 115–145.
- 668 Solomon, S. H., Medaglia, J. D., & Thompson-Schill, S. L. (2019). Implementing a concept network model.  
669 *Behavior Research Methods*, 51, 1717–1736.
- 670 Spearman, C. (1904). General intelligence, objectively determined and measured. *American Journal of  
671 Psychology*, 15, 201–292.
- 672 Sporns, O., & Honey, C. J. (2006). Small worlds inside big brains. *Proceedings of the National Academy of  
673 Science USA*, 103(51), 19219–19220.
- 674 Thompson, W. H., Richter, C. G., Plavén-Sigray, P., & Fransson, P. (2018). Simulations to benchmark  
675 time-varying connectivity methods for fMRI. *PLoS Computational Biology*, 14(5), e1006196.
- 676 Tipping, M. E., & Bishop, C. M. (1999). Probabilistic principal component analysis. *Journal of Royal Statistical  
677 Society, Series B*, 61(3), 611–622.
- 678 Toker, D., & Sommer, F. T. (2019). Information integration in large brain networks. *PLoS Computational  
679 Biology*, 15(2), e1006807.
- 680 Tong, F., & Pratte, M. S. (2012). Decoding patterns of human brain activity. *Annual Review of Psychology*, 63,  
681 483–509.
- 682 Turk-Browne, N. B. (2013). Functional interactions as big data in the human brain. *Science*, 342, 580–584.
- 683 van der Maaten, L. J. P., & Hinton, G. E. (2008). Visualizing high-dimensional data using t-SNE. *Journal of  
684 Machine Learning Research*, 9, 2579–2605.
- 685 Vidaurre, D., Abeysuriya, R., Becker, R., Quinn, A. J., Alfaro-Almagro, F., Smith, S. M., & Woolrich, M. W.  
686 (2018). Discovering dynamic brain neworks from big data in rest and task. *NeuroImage*, 180, 646–656.
- 687 Zar, J. H. (2010). *Biostatistical analysis*. Prentice-Hall/Pearson.
- 688 Zheng, M., Allard, A., Hagmann, P., & Serrano, M. A. (2019). Geometric renormalization unravels self-  
689 similarity of the multiscale human connectome. *arXiv*, 1904.11793.
- 690 Zou, Y., Donner, R. V., Marwan, N., Donges, J. F., & Kurths, J. (2019). Complex network approaches to  
691 nonlinear time series analysis. *Physics Reports*, 787, 1–97.